Title

Molecular beam epitaxy of phase-pure antiperovskite Sr_3SnO thin films

Journal

Applied Physics Letters, 119(16)

ISSN

0003-6951 1077-3118

Authors

Wu, Wangzhou
Combs, Nicholas G
Stemmer, Susanne

Publication Date

2021-10-18

DOI

10.1063/5.0068187

Peer reviewed

Applied Physics Letters

Molecular beam epitaxy of phase-pure antiperovskite Sr_3SnO thin films

Cite as: Appl. Phys. Lett. **119**, 161903 (2021); https://doi.org/10.1063/5.0068187
Submitted: 23 August 2021 • Accepted: 01 October 2021 • Published Online: 18 October 2021

Wangzhou Wu, Nicholas G. Combs and Susanne Stemmer

AIP Publishing

Applied Physics Letters ARTICLE scitation.org/journal/apl

Molecular beam epitaxy of phase-pure antiperovskite Sr_3SnO thin films

Cite as: Appl. Phys. Lett. **119**, 161903 (2021); doi: 10.1063/5.0068187
Submitted: 23 August 2021 · Accepted: 1 October 2021 ·
Published Online: 18 October 2021

View Online Export Citation CrossMark

Wangzhou Wu, Nicholas G. Combs, and Susanne Stemmer[a)]

AFFILIATIONS

Materials Department, University of California, Santa Barbara, California 93106-5050, USA

[a)]Author to whom correspondence should be addressed: stemmer@mrl.ucsb.edu

ABSTRACT

The antiperovskite oxide Sr_3SnO has attracted substantial interest due to its topologically non-trivial band structure. Sr-deficient $Sr_{3-x}SnO$ can become superconducting, making it a candidate intrinsic topological superconductor. Here, we show that epitaxial, phase-pure $Sr_{3-x}SnO$ films can be synthesized by molecular beam epitaxy (MBE) using solid Sr and SnO_2 sources. We show that Sn-rich growth conditions result in a large amount of a Sn-rich impurity phase, which is challenging to detect in x-ray diffraction. Carrier densities and the amount of the impurity phase change systematically with the growth conditions, indicating that MBE provides excellent control over the films' stoichiometry. We discuss the electrical properties, including quantum interference phenomena, which support the topological nature of the films.

Antiperovskite oxides with the chemical formula A_3BO, where A is an alkaline earth metal such as Ca, Ba, or Sr, and B stands for Sn or Pb, crystallize into a structure in which the positions of the A^{2+} and O^{2-} ions are exchanged relative to the well-known perovskite structure.[1,2] The metal ion on the B-site adopts an unusual 4-formal valence state.[1,2] The unusual electronic configuration is reflected in the band structures of these oxides, which feature band inversions, Dirac fermions, and topologically non-trivial Chern numbers.[3–8] For example, Sr_3SnO is a three-dimensional Dirac semimetal with a small bandgap (so is more correctly described as a topological crystalline insulator) that features six Dirac nodes along each of the six Γ-X directions.[4] Moreover, Sr-deficient $Sr_{3-x}SnO$ is also superconducting.[9–11] The unusual combination of superconductivity and the topological band structure makes $Sr_{3-x}SnO$ a candidate intrinsic topological superconductor,[7] which is very rare. Thus far, however, superconductivity has only been observed in highly Sr-deficient $Sr_{3-x}SnO$ polycrystalline samples that also contain secondary phases.[9–11] The role of these impurity phases in observations of superconductivity in $Sr_{3-x}SnO$ remains poorly understood.

Phase-pure, thin films of $Sr_{3-x}SnO$ are of great interest for obtaining an improved understanding of its properties. Recently, molecular beam epitaxy (MBE) of Sr_3SnO and Sr_3PbO films has been reported.[12–14] These studies relied on x-ray diffraction (XRD) to ascertain phase purity of the films. Impurity phases in thin films can, however, be difficult to detect in XRD, especially if they are randomly oriented or poorly crystallized. Characterization of Sr_3SnO films by electron microscopy techniques is challenging, because they are extremely reactive in air.

Here, we use a combination of XRD and *in situ* scanning electron microscopy (SEM) in a focused ion beam (FIB) instrument to investigate Sr_3SnO films grown by MBE. We show that phase-pure Sr_3SnO films can be grown. Under non-stoichiometric growth conditions, however, XRD is not able to detect large amount of a secondary phase even in films as thick as 850 nm. Moreover, transport properties are also surprisingly insensitive to the presence of a Sn-rich impurity phase.

Sr_3SnO films were grown on (001) $LaAlO_3$ substrates in an oxide MBE system (GEN 930, Vecco Instruments), by co-evaporation of high-purity elemental Sr (4N, Sigma Aldrich) and SnO_2 (4N, Kurt J. Lesker) from solid source effusion cells (see the supplementary material, Fig. S1 for a schematic of the sample structure). The solid SnO_2 source supplies primarily SnO and O_2[15] and facilitates the growth of high-quality stannates by providing pre-oxidized Sn.[16,17] Sr_3SnO is cubic with a lattice parameter of $a = 5.12$ Å.[1] The lattice mismatch between Sr_3SnO and $LaAlO_3$ [$a = 3.79$ Å (Ref. 18)] is about −5%, assuming that Sr_3SnO grows with 45° in-plane rotation $\left(5.12\ \text{Å}/\sqrt{2} = 3.62\ \text{Å}\right)$, and we, therefore, expect epitaxial films to be fully relaxed. Substrates were backed with 350 nm Mo to improve the heat transfer from the substrate heater and were cleaned in acetone and isopropanol before loading into the entry/exit chamber. Prior to growth, the substrate was heated up to 650 °C (thermocouple) and kept for about 10 min. The films' stoichiometry was controlled by keeping the Sr flux

constant and varying the flux from the SnO_2 cell. Here, the Sr beam equivalent pressure (BEP) was 5.0×10^{-7} Torr, while the BEP from the SnO_2 cell was varied between 4.0×10^{-8} and 2.4×10^{-7} Torr. The films discussed in the main text were grown with Sr/SnO_x BEP ratios of 12.5, 8.7, 4.2, and 2.1. The corresponding growth rates of these films were 140, 200, 480, and 850 nm/h, respectively, and are, therefore, SnO_x-flux limited. Film growth was monitored using *in situ* reflection high-energy electron diffraction (RHEED). Due to their extreme air sensitivity, samples for high-resolution XRD and FIB/SEM (FEI Helios dual beam) were protected by a layer of either TiO_2 or ZrO_2. These capping layers were grown at 375 °C in the same MBE chamber using titanium tetra isopropoxide and zirconium tert-butoxide as source materials.[19,20]

An additional Pt protection layer was deposited on a $15 \times 2\ \mu m^2$ rectangular area for cross-sectional SEM in the FIB instrument. Samples were imaged in the immersion mode using secondary electrons with sample surface tilted 52° relative to the electron beam. Films used for electrical measurements were uncapped. To avoid air-exposure, In contacts were soldered in van der Pauw geometry inside a N_2 glove bag. The exposed sample surface was then covered by a layer of Apiezon-N grease. (Magneto-)transport measurements were performed in a physical property measurement system (Quantum Design) between 280 and 2 K. The thicknesses of the films used for electrical measurement was about 300 nm. The measured longitudinal magnetoresistance was symmetrized to cancel out the contribution from the Hall effect: $R_{xx}^{sym}(B) = \frac{R_{xx}(B)+R_{xx}(-B)}{2}$, where R_{xx} is the longitudinal resistance and B is the magnetic field and inverted to convert it into magnetoconductance.

Figure 1 shows RHEED patterns of Sr_3SnO films grown with different Sr/SnO_x BEP ratios [from (a) to (d): 12.5, 8.7, 4.2, and 2.1, respectively]. Spotty features are observed in all patterns, indicating three-dimensional (island) growth. The spotty-ness in RHEED is much more pronounced for the films grown with Sr/SnO_x BEP ratios of 4.2 and 2.1, compared to those grown under less Sn-rich conditions. As discussed below, the film grown with the highest Sr/SnO_x BEP ratio [Fig. 1(a)] is phase pure.

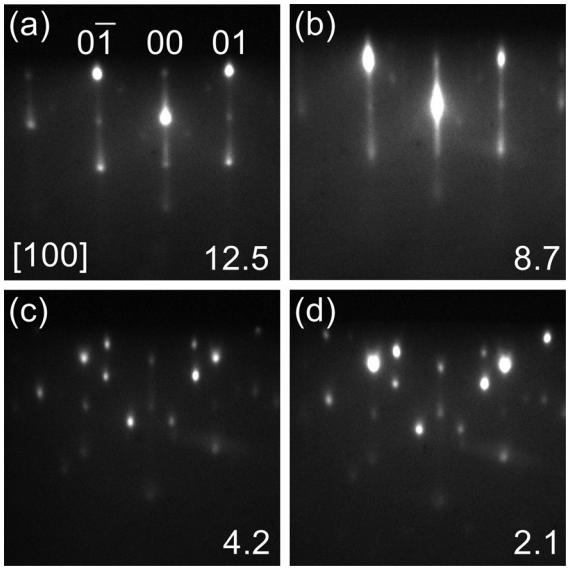

FIG. 1. RHEED patterns of Sr_3SnO films grown by MBE with four different Sr/SnO_x BEP ratios: (a) 12.5, (b) 8.7, (c) 4.2, and (d) 2.1, as indicated by the labels. The $LaAlO_3$ substrate temperature was 650 °C for all films.

Figure 2 shows on-axis XRD scans of the films shown in Fig. 1. All reflections can be assigned to a (001)-oriented Sr_3SnO film and the substrate, with no additional reflections detected for all growth parameters. One issue is that SrO, which has a lattice constant close to that of Sr_3SnO, is a possible impurity phase in Sr_3SnO.[10] Sr_3SnO can be distinguished from SrO by the presence of 00l (l = odd) reflections, which are forbidden in face-centered SrO. All films show 001 and 003 reflections [see also Fig. 2(b)]. The greater intensity of the 001 reflections of films grown with lower Sr/SnO_x BEP ratios is due to increased growth rate at higher SnO_x fluxes, which results in thicker films for similar growth times (see Fig. 3 for the films' thicknesses). The presence of 00l (l = odd) reflections is, however, not sufficient to rule out SrO impurities. In addition, as mentioned above, impurity phases may be difficult to detect in XRD, especially if they are poorly crystallized.

To gain a better understanding of the phase purity of the films, we show in Fig. 3 cross-section SEM images of the same films. Images of the film grown with a Sr/SnO_x BEP ratio of 12.5 confirm the absence of secondary phases [Fig. 3(a)]. In conjunction with the XRD data, this shows that this film is phase-pure Sr_3SnO.

In contrast, films grown under Sn-rich conditions, shown in Figs. 3(b)–3(d), contain a secondary phase that appears as a columnar, dark region in SEM. The volume fraction of the secondary phase increases with an increasing SnO_x flux and corresponds to 25%, 30%, and 45%, respectively, for the films shown in Figs. 3(b)–3(d). The systematic increase in volume fraction indicates that the secondary phase is a Sn-rich alloy (not SrO). Importantly, the Sn-rich impurity phase is not detected in XRD even for films as thick as 850 nm. Reflections associated with the Sn-rich secondary phase can only be detected in XRD for extremely Sn-rich growth conditions, when the Sn-rich phase adopts a distinctly different morphology (see the supplementary material). We conclude that XRD alone is insufficient to ascertain phase-

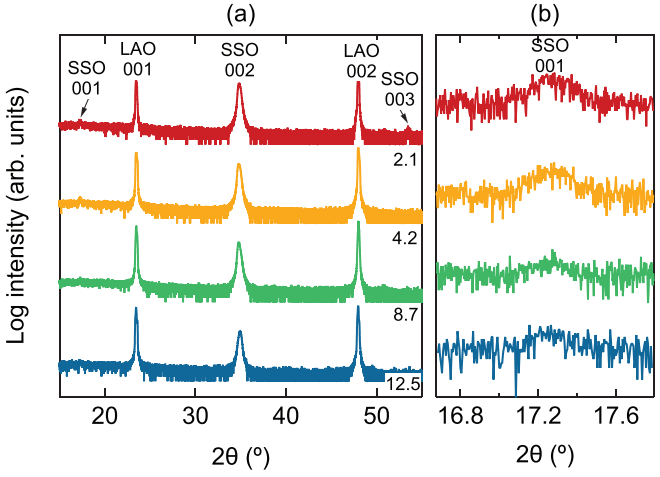

FIG. 2. (a) XRD 2θ-ω scans of Sr_3SnO films grown on (001) $LaAlO_3$ substrates with different Sr/SnO_x BEP ratios, as indicated by the labels. (b) High resolution XRD 2θ-ω scan around the 001 reflection of Sr_3SnO. SSO: Sr_3SnO and LAO: $LaAlO_3$.

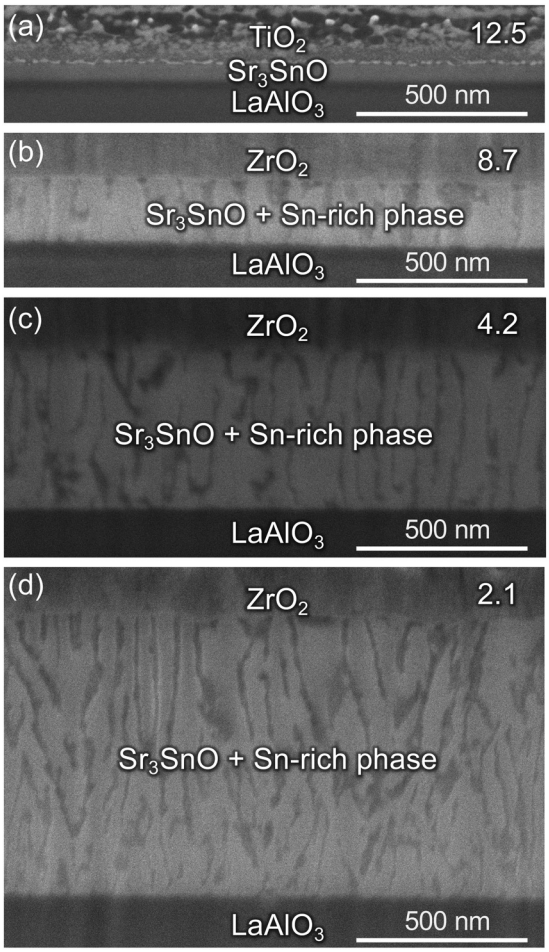

FIG. 3. Cross-sectional SEM images of Sr_3SnO films grown on $LaAlO_3$ with four different Sr/SnO_x BEP ratios: (a) 12.5, (b) 8.7, (c) 4.2, and (d) 2.1. The films are capped by either TiO_2 (a) or ZrO_2 (b)–(d) to prevent the reaction in air.

purity of Sr_3SnO films even in cases where a secondary, Sn-rich phase constitutes a large volume fraction.

We next turn to the electrical properties. Figure 4 shows the sheet resistance, R_s, as a function of temperature for two films grown with Sr/SnO_x BEP ratios of 12.5 (phase pure film) and 4.2 (Sn-rich), respectively. Both films show metallic behavior followed by an upturn in resistance at low temperatures, similar to Sr_3SnO films reported in the literature,[13,21] and consistent with the negligible bandgap of Sr_3SnO. Both films are p-type (see the supplementary material, Fig. S3). Their carrier concentrations are $9.6 \times 10^{18}\,cm^{-3}$ and $1.5 \times 10^{19}\,cm^{-3}$, respectively. The carrier density in the films is well below the doping needed to induce superconductivity in $Sr_{3-x}SnO$, which requires Sr deficiency corresponding to at least $x = 0.35$.[10] Hole doping has been attributed to the presence of Sr vacancies.[9,10] The higher carrier density in the film grown under Sn-rich (Sr-poor) conditions is consistent with this interpretation. We note, however, that an increase of >200% in the SnO_x flux only increases the carrier density by 50%. This is because the change in growth conditions results not only in increased Sr deficiency of $Sr_{3-x}SnO$ but also in the formation of Sn-rich phases,

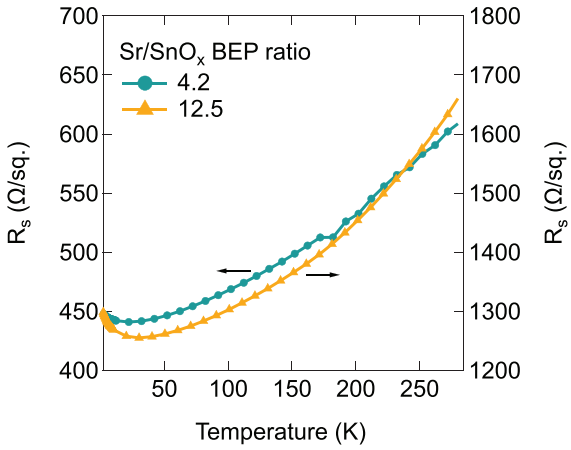

FIG. 4. Sheet resistance measured between 280 and 2 K of two Sr_3SnO films grown with different Sr/SnO_x BEP ratios of 12.5 and 4.2, respectively.

as discussed above. Comparing the two films, we see that the temperature dependence of R_s is qualitatively similar, while the higher R_s in the phase pure film is due to its lower carrier density. Both of these observations indicate that the secondary phase present in the Sn-rich film has surprisingly little influence on transport, likely because it is not percolated in this film.

As shown in Fig. 5(a), phase pure films exhibit negative magnetoconductance at low temperatures under perpendicular magnetic fields (B). The magnetoconductance data at 50, 10, and 2 K can be fitted [see Fig. 5(b)] to the Hikami–Larkin–Nagaoka equation for weak antilocalization (WAL) in the strong spin–orbit coupling limit[22]

$$\Delta G_{xx} = \alpha \frac{e^2}{h}\left[\ln\left(\frac{B_\varphi}{B}\right) - \psi\left(\frac{B_\varphi}{B} + \frac{1}{2}\right)\right], \quad (1)$$

where e is the elementary charge, h is Planck's constant, B_φ is a phase coherence characteristic field, and ψ is the digamma function. The pre-factor α takes the values -1 for weak localization and $^1/_2$ for WAL. The extracted values for α are 0.08 (50 K), 0.30 (10 K), and 0.45 (2 K). The corresponding values for the phase coherence length, given as $l_\varphi = \sqrt{h/(8\pi e B_\varphi)}$, are 44, 87, and 146 nm. Strong WAL has previously been observed in Sr_3SnO films[14] and perovskites containing Sn.[23] The WAL is commonly observed in topological insulators and semimetals,[24,25] which can be understood to be the result of a π Berry phase associated with a spin-momentum-locked Fermi surface[26] or strong spin–orbit coupling.[22] The fact that α approaches 0.5 at 2 K points to a Berry phase of π is consistent with a topological material. We note that the resistance upturn seen in the temperature-dependence of R_s (Fig. 4) is characteristic of weak localization, not WAL. Similar apparently contradictory behavior has been observed in topological insulators.[24,27] One possible explanation is that electron correlation effects are dominating the temperature dependence (Altshuler–Aronov correction[28]) while the magnetoconductance is dominated by WAL.[24,27]

In summary, we have shown that phase-pure conducting $Sr_{3-x}SnO$ films can be grown by MBE, and their carrier densities (hole doping) can be controlled via the MBE growth parameters. Sn-rich growth conditions, which are needed for the high doping

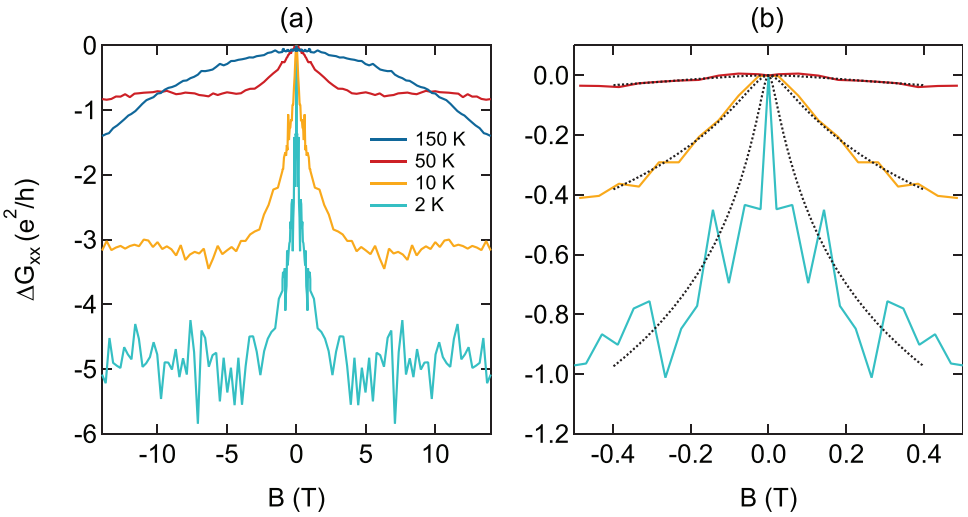

FIG. 5. (a) Magnetoconductance of the phase pure film grown with a Sr/SnO_x BEP ratio of 12.5 measured between –14 and 14 T at different temperatures. (b) A zoomed-in subset of the data in (a) at lower magnetic fields. The dotted lines are a Hikami–Larkin–Nagaoka fit. The data are symmetrized.

concentrations required for superconductivity in $Sr_{3-x}SnO$, result in films that contain a large amount of a Sn-rich secondary phase. These secondary phases are difficult to detect in XRD but can readily be observed in electron microscopy images. Phase-pure films with carefully controlled doping densities, as afforded by MBE, are an ideal platform for future studies of topological transport phenomena.

See the supplementary material for a schematic of the sample structure, XRD and SEM images of extremely Sn-rich films, and the Hall measurements of the films shown in Fig. 4.

The authors thank Hanbyeol Jeong and Kurt Olsson for assistance with the glove bag transfer. This work was supported by the U.S. Department of Energy (Award No. DE-SC0020305) and the MURI program of the Army Research Office (Grant No. W911NF-16-1-0361). N.G.C. acknowledges support through the UCSB Quantum Foundry, which is supported by the National Science Foundation (Award No. DMR-1906325). This work made use of the MRL Shared Experimental Facilities, which are supported by the MRSEC Program of the U.S. National Science Foundation under Award No. DMR 1720256.

AUTHOR DECLARATIONS

Conflict of Interest

The authors have no conflicts to disclose.

DATA AVAILABILITY

The data that support the findings of this study are available within the article.

REFERENCES

[1]A. Widera and H. Schafer, "Transitional forms between Zintl phases and real salts—Compounds A_3BO (A = Ca, Sr, Ba and B-Sn, Pb)," Mater. Res. Bull. **15**, 1805–1809 (1980).
[2]J. Nuss, C. Muhle, K. Hayama, V. Abdolazimi, and H. Takagi, "Tilting structures in inverse perovskites, M_3TtO (M = Ca, Sr, Ba, Eu; Tt = Si, Ge, Sn, Pb)," Acta Crystallogr. B **71**, 300–312 (2015).
[3]T. Kariyado and M. Ogata, "Three-dimensional Dirac electrons at the Fermi energy in cubic inverse perovskites: Ca_3PbO and its family," J. Phys. Soc. Jpn. **80**, 083704 (2011).
[4]T. H. Hsieh, J. W. Liu, and L. Fu, "Topological crystalline insulators and Dirac octets in antiperovskites," Phys. Rev. B **90**, 081112 (2014).
[5]Y. Obata, R. Yukawa, K. Horiba, H. Kumigashira, Y. Toda, S. Matsuishi, and H. Hosono, "ARPES studies of the inverse perovskite Ca_3PbO: Experimental confirmation of a candidate 3D Dirac fermion system," Phys. Rev. B **96**, 155109 (2017).
[6]A. Ikeda, T. Fukumoto, M. Oudah, J. N. Hausmann, S. Yonezawa, S. Kobayashi, M. Sato, C. Tassel, F. Takeiri, H. Takatsu, H. Kageyama, and Y. Maeno, "Theoretical band structure of the superconducting antiperovskite $Sr_{3-x}SnO$," Physica B **536**, 752–756 (2018).
[7]T. Kawakami, T. Okamura, S. Kobayashi, and M. Sato, "Topological crystalline materials of $J = 3/2$ electrons: Antiperovskites, Dirac points, and high winding topological superconductivity," Phys. Rev. X **8**, 041026 (2018).
[8]Y. Fang and J. Cano, "Higher-order topological insulators in antiperovskites," Phys. Rev. B **101**, 245110 (2020).
[9]M. Oudah, A. Ikeda, J. N. Hausmann, S. Yonezawa, T. Fukumoto, S. Kobayashi, M. Sato, and Y. Maeno, "Superconductivity in the antiperovskite Dirac-metal oxide $Sr_{3-x}SnO$," Nat. Commun. **7**, 13617 (2016).
[10]M. Oudah, J. N. Hausmann, S. Kitao, A. Ikeda, S. Yonezawa, M. Seto, and Y. Maeno, "Evolution of superconductivity with Sr-deficiency in antiperovskite oxide $Sr_{3-x}SnO$," Sci. Rep. **9**, 1831 (2019).
[11]A. Ikeda, Z. Guguchia, M. Oudah, S. Koibuchi, S. Yonezawa, D. Das, T. Shiroka, H. Luetkens, and Y. Maeno, "Penetration depth and gap structure in the antiperovskite oxide superconductor $Sr_{3-x}SnO$ revealed by mu SR," Phys. Rev. B **101**, 174503 (2020).
[12]D. Samal, H. Nakamura, and H. Takagi, "Molecular beam epitaxy of three-dimensional Dirac material Sr_3PbO," APL Mater. **4**, 076101 (2016).
[13]Y. J. Ma, A. Edgeton, H. Paik, B. D. Faeth, C. T. Parzyck, B. Pamuk, S. L. Shang, Z. K. Liu, K. M. Shen, D. G. Schlom, and C. B. Eom, "Realization of epitaxial thin films of the topological crystalline insulator Sr_3SnO," Adv. Mater. **32**, 2000809 (2020).
[14]H. Nakamura, D. Huang, J. Merz, E. Khalaf, P. Ostrovsky, A. Yaresko, D. Samal, and H. Takagi, "Robust weak antilocalization due to spin-orbital entanglement in Dirac material Sr_3SnO," Nat. Commun. **11**, 1161 (2020).
[15]R. H. Lamoreaux, D. L. Hildenbrand, and L. Brewer, "High-temperature vaporization behavior of oxides. II. Oxides of Be, Mg, Ca, Sr, Ba, B, Al, Ga, In, Tl, Si, Ge, Sn, Pb, Zn, Cd, and Hg," J. Phys. Chem. Ref. Data **16**, 419–443 (1987).
[16]S. Raghavan, T. Schumann, H. Kim, J. Y. Zhang, T. A. Cain, and S. Stemmer, "High-mobility $BaSnO_3$ grown by oxide molecular beam epitaxy," APL Mater. **4**, 016106 (2016).

[17]N. G. Combs, W. Z. Wu, and S. Stemmer, "Stoichiometry control in molecular beam epitaxy of $BaSnO_3$," Phys. Rev. Mater. **4**, 014604 (2020).
[18]S. Geller and V. B. Bala, "Crystallographic studies of perovskite-like compounds. II. Rare earth aluminates," Acta Crystallogr. **9**, 1019–1025 (1956).
[19]B. Jalan, R. Engel-Herbert, J. Cagnon, and S. Stemmer, "Growth modes in metal-organic molecular beam epitaxy of TiO_2 on r-plane sapphire," J. Vac. Sci. Technol. A **27**, 230–233 (2009).
[20]R. Engel-Herbert, Y. Hwang, J. Cagnon, and S. Stemmer, "Metal-oxide-semiconductor capacitors with ZrO_2 dielectrics grown on $In_{0.53}Ga_{0.47}As$ by chemical beam deposition," Appl. Phys. Lett. **95**, 062908 (2009).
[21]D. Huang, H. Nakamura, and H. Takagi, "Planar Hall effect with sixfold oscillations in a Dirac antiperovskite," Phys. Rev. Res. **3**, 013268 (2021).
[22]S. Hikami, A. I. Larkin, and Y. Nagaoka, "Spin-orbit interaction and magnetoresistance in the two dimensional random system," Prog. Theor. Phys. **63**, 707–710 (1980).
[23]K. Nasyedkin, I. King, L. Zhang, P. Chen, L. Wang, R. J. Staples, R. R. Lunt, and J. Pollanen, "Extraordinary phase coherencelength in epitaxial halide perovskites," iScience **24**, 102912 (2021).
[24]J. H. Bardarson and J. E. Moore, "Quantum interference and Aharonov–Bohm oscillations in topological insulators," Rep. Prog. Phys. **76**, 056501 (2013).
[25]H.-Z. Lu and S.-Q. Shen, "Quantum transport in topological semimetals under magnetic fields," Front. Phys. **12**, 127201 (2017).
[26]T. Ando, T. Nakanishi, and R. Saito, "Berry's phase and absence of back scattering in carbon nanotubes," J. Phys. Soc. Jpn. **67**, 2857–2862 (1998).
[27]H.-Z. Lu and S.-Q. Shen, "Finite-temperature conductivity and magnetoconductivity of topological insulators," Phys. Rev. Lett. **112**, 146601 (2014).
[28]B. L. Altshuler and A. G. Aronov, "Zero bias anomaly in tunnel resistance and electron-electron interaction," Solid State Commun. **30**, 115–117 (1979).